First-principles comparative study of Cr migration in O3 and O/P hybrid-phased math xmlns="http://www.w3.org/1998/Math/MathML">msub>mi >NaCrO/mi>mn>2/mn>/msub>/math>

Jialiang Wei, Leon Shaw, and Wei Chen

Phys. Rev. Materials **6**, 095403 — Published 28 September 2022

DOI: 10.1103/PhysRevMaterials.6.095403

First-principles comparative study of Cr migration in O3 and O/P hybrid-phased $NaCrO_2$

Jialiang Wei, Leon Shaw and Wei Chen*

Department of Mechanical, Materials and Aerospace Engineering, Illinois Institute of Technology, Chicago, Illinois 60616, USA

Abstract

In layered Na transition metal (TM) oxides, TM migration usually occurs at highly charged states and severely deteriorates the capacity and reversibility. Meanwhile, the formation of hybrid phases with the intergrowth of octahedral (O-type) and prismatic (P-type) Na layers also takes place at highly charged states. These hybrid phases are often more stable than simple O3 or P3 stackings. However, little is known about the mechanism and impact of TM migration in these hybrid phases. In this work, a comparative first-principles study is performed to understand the connections between structural changes and Cr migration in layered O3 and hybrid-phased $NaCrO_2$. After Cr migration, the hybrid-phased $NaCrO_2$ suffers from greater layer shrinkage than the O3 phase. Three factors affect the Cr migration energy E_{mig}: the Na concentration, local 3D configurations, and 2D in-plane geometries. Low Na concentrations and certain local 3D configurations facilitate the Cr migration. The Cr migration barriers in both O3 and hybrid-phased $NaCrO_2$ are positively correlated with the Cr E_{mig}. The Cr migration in 17 doped O3 and hybrid-phased $NaCrO_2$ is surveyed. In these doped $NaCrO_2$, a more uniform distribution of the Cr–O bond lengths usually suggests suppressed Cr migration. Optimal dopants for suppressing Cr migration are identified by considering E_{mig} for both Cr and the dopant. Our comparative study on Cr migration in O3 and hybrid-phased $NaCrO_2$ reveals the significant role of hybrid-phased structures in the development of layered cathode materials.

1. Introduction

Compared with other cathode materials for sodium-ion batteries (*e.g.*, Prussian blue analogues and polyanion compounds), layered Na transition metal (TM) oxides with the stoichiometry of $NaTMO_2$ (TM=Ti, V, Cr, Mn, Fe, Co, Ni) represent a class of cathode materials with high theoretical volume capacity and rate capability. [1–9] Generally, layered Na TM oxides can be classified into two subgroups O3 and P3 depending on the coordination environment of Na^+. The notation O3 (or P3) stands for octahedrally (or prismatically) coordinated alkali metals with an ABCABC (or AABBCC) stacking of the oxygen layers. [10] The prime in O'3 or P'3 indicates the existence of monoclinic distortion. Due to the structural and phase changes at highly charged (*i.e.*, highly desodiated) states, $NaTMO_2$ cannot fully utilize their superior theoretical capacity. For example, O3 $NaCrO_2$ is only electrochemically active when no more than 50 at.% Na are extracted in the first cycle. [3] Thus, understanding the structural and phase changes at highly charged states is critical for realizing high reversible capacity in layered Na TM oxides.

In layered cathode materials, the TM migration accompanied with the alkali metal extraction is pervasive. The TM migration causes irreversible capacity loss by introducing severe layer shrinkage and blocking the transport of alkali ions. [11,12] The phenomenon is severe in Li cathodes because the Li–TM mixing can be thermodynamically favorable due to their close cation sizes. [13] For example, in Ni-rich layered $LiNi_{0.7}(MnCo)_{0.3}O_2$, the Li–Ni mixing is largely driven by the similar size of Ni^{2+} (0.69 Å) and Li^+ (0.76 Å). [14] In layered Na TM oxides, especially when TM = Cr, Fe, and Mn and after around 50 at.% Na are extracted, the TM migration is also prevalent, limiting their reversible capacity. [12] In O3 Na_xFeO_2, the migration energy of Fe is only 0.8 eV at x=1/3 [15] and the Jahn-Teller active Fe^{4+} can further assist the Fe migration from distorted $Fe^{4+}O_6$. Theoretical calculations have shown a low Cr migration energy of –0.01 eV in the CrO_2 slab when Na is fully extracted. [13] More specifically, experimental observations indicate Cr migration occurs in O3 Na_xCrO_2 when x<0.4 before it transforms into fully desodiated rock-salt phase CrO_2. [13,16] These previous studies reveal the particularly high likelihood of TM migration in layered TM oxides at highly charged states.

In addition to TM migration, the gliding of oxygen layers may lead to a series of complicated phase evolution in layered Na TM oxides. [17] For example. Na_xCoO_2 ($0.56<x<1$) experiencing the O3→O'3→P'3 phase transformation has been identified during the electrochemical Na extraction. A two-phase mixture exists between stable ground states. [18] However, rather than a two-phase mixture,

a recent study unveils the intergrowth of octahedral (O-type) and prismatic (P-type) Na layers during the phase transformation for many layered Na TM oxides at highly charged states. [19] The intergrowth of different layers forms hybrid-phased compounds. The first reported hybrid-phased TM oxide is $Na_{0.667}(Fe_{0.5}Mn_{0.5})O_2$. After being charged to 4.2 V, the TM oxide exhibits an alternating O-type and P-type stacking along the *c*-axis as an OP4 phase, [20] where the selective Na extraction from the P stacked layers creates a Na-rich O-type layer and a Na-poor P-type layer. Another 'Z' hybrid phase, which also shows the co-existence of O-type and P-type phases, was recently discovered at highly charged states of layered Na compounds. [21,22] Little is known about the TM migration in these hybrid-phased Na TM oxides at highly charged states. Theoretical calculations of the hybrid phased $Na_{0.25}Fe_{0.5}Ni_{0.5}O_2$ suggest the difference in the TM–TM interlayer distance can be as large as 0.1 Å between the O-type and P-type stacking. [16] The Fe migration into the O-type Na layer further reduces its interlayer distance because the high valence Fe^{4+} introduces stronger cation–anion attraction than Na^+. [17] More Fe seem to migrate into the Na layer when the Na interlayer distance is small. [23]

In this study, Na_xCrO_2 ($x \leq 0.5$) is selected as a representative system to understand the TM migration at highly charged states. We use first-principles density functional theory (DFT) calculations to reveal the structural and chemical factors for Cr migration in O3 and hybrid-phased O2P $NaCrO_2$ and potential strategies to suppress the migration. [13,16,24] Our calculations indicate that hybrid-phased O2P $NaCrO_2$ is more stable than O3 at highly desodiated states. We discover a new configuration with a low Cr migration energy in O2P $NaCrO_2$. The Cr-migration pathway is studied with the climbing image nudged elastic band (CI-NEB) method and favorable local environments for Cr migration are discussed. [25] Cr migration is related to the disproportion reaction of unstable Cr^{4+} into stable Cr^{3+} and Cr^{6+} because the high valence Cr^{6+} prefers a tetrahedral coordination. [26] Introducing metallic dopants with large sizes or high valence states can suppress Cr migration in $NaCrO_2$. [24] Lastly, the effect of doping on Cr migration is studied and we identify promising dopants that can effectively suppress Cr migration.

2. Methods

Based on the low-energy in-plane Na-vacancy orderings from a prior study, [25] we first constructed layered O3 and P3 Na_xCrO_2 configurations at Na concentrations x = 1/7, 1/4, 1/3, 2/5, and 1/2 with supercells containing 66, 39, 30, 60, and 42 atoms, respectively. A zig-zagged in-plane structure was used for x = 2/5 and 1/2 where two or more Na atoms exist in a single Na layer of the supercell. The

hybrid-phased O2P and OP2 structures are obtained by gliding one and two oxygen layers from the O3 structures. Then, Cr-migrated configurations were screened by their electrostatic energy with Ewald summation, and DFT calculations were performed to get accurate total energy of low electrostatic energy structures. [27,28] First-principles calculations were conducted using the Vienna *ab initio* simulation package (VASP) with the projector augmented-wave (PAW) method. [29–31] The exchange-correlation energy was described using the Perdew-Burke-Ernzerhof (PBE) generalized-gradient approximation (GGA). [32,33] The on-site Coulomb interactions for localized TM 3d orbitals were applied by the Hubbard *U* parameters to correct the total energy of TM oxides from PBE. [34] The *U* values were determined by the Material Project by fitting the formation enthalpies of binary TM oxides to experimental values. [35,36] The effective *U* value for Cr, V, Mn, Fe, Co, Ni, and Mo were 3.7, 3.25, 3.9, 5.3, 3.32, 6.2, and 4.38 eV, respectively. [37] A plane-wave cut off energy of 520 eV and Gamma-centered **k**-point meshes with at least 1500 **k**-points per reciprocal atom were used. Spin-polarized calculations were initialized with high-spin, except for the Co dopant. [38] The total energy and force were converged to 10^{-5} eV per supercell and 0.02 eV/ Å, respectively. We compared the total energies of $NaCrO_2$ in the pristine state and post Cr migration with both ferromagnetic and anti-ferromagnetic ordering. Because the total energy differences between these magnetic orderings are only several meV/atom, the ferromagnetic initialization was used consistently in the study.

The Cr-migration energy E_{mig} is defined as the energy difference between the pristine structure and the structure with Cr migrated to either the tetrahedral or the octahedral site in the Na layer. [13] A low Cr E_{mig} suggests a higher tendency for Cr to migrate.

$$E_{\text{mig}} = E_{\text{Cr migrated}} - E_{\text{pristine}} \quad (1)$$

To obtain the energy barrier of Cr migration, the CI-NEB method was used with a force convergence criterion of 0.02 eV/Å. [39] The Cr-migration barrier ΔE is evaluated as

$$\Delta E = E_{\text{max}} - E_{\text{initial}} \quad (2)$$

where E_{max} is the energy of the image with the highest energy along the minimum energy pathway and E_{initial} is the energy of the initial state.

Doped structures were generated by substituting one Cr atom with a dopant atom in a low-energy $Na_{1/7}CrO_2$ supercell, giving a dopant concentration of 1/27. Experimental evidence shows the layered framework of Na_xCrO_2 can exist at a dilute Na concentration $x \approx 0.04$. [16] The relative stability of doped $NaCrO_2$ is evaluated by the energy above the hull E_{hull}, which is the energy above the tie-line

between adjacent ground states. All relevant stable compounds were retrieved from the Materials Project and recalculated with consistent parameters. [36,40]

3. Cr migration in hybrid O2P phases

3.1 The Cr-migration energy

In Fig. 1(a), the crystal structure of O3, P3 and hybrid-phased O2P $NaCrO_2$ is illustrated. The Cr migration into the Na layer L2 through a triangular face of oxygen atoms is illustrated in Fig. 1(b) and (c). We focus on studying the Cr migration to the tetrahedral site Cr(tet) because a direct migration of TM to an octahedral site Cr(oct) through an octahedral edge is kinetically unfavorable with an energy barrier over 2 eV. [41] A recent study also pointed out that the migration to Cr(tet) is the first and rate-limiting step in the Cr migration process. [42] We first enumerated possible Na configurations in the Na layer L1 and screened them by the Ewald summation to estimate the electrostatic interactions of partially desodiated Na_xCrO_2 configurations. [27,28,43] For each pristine structure, 10 low-energy Cr-migrated configurations were then optimized by DFT to find the Cr E_{mig}.

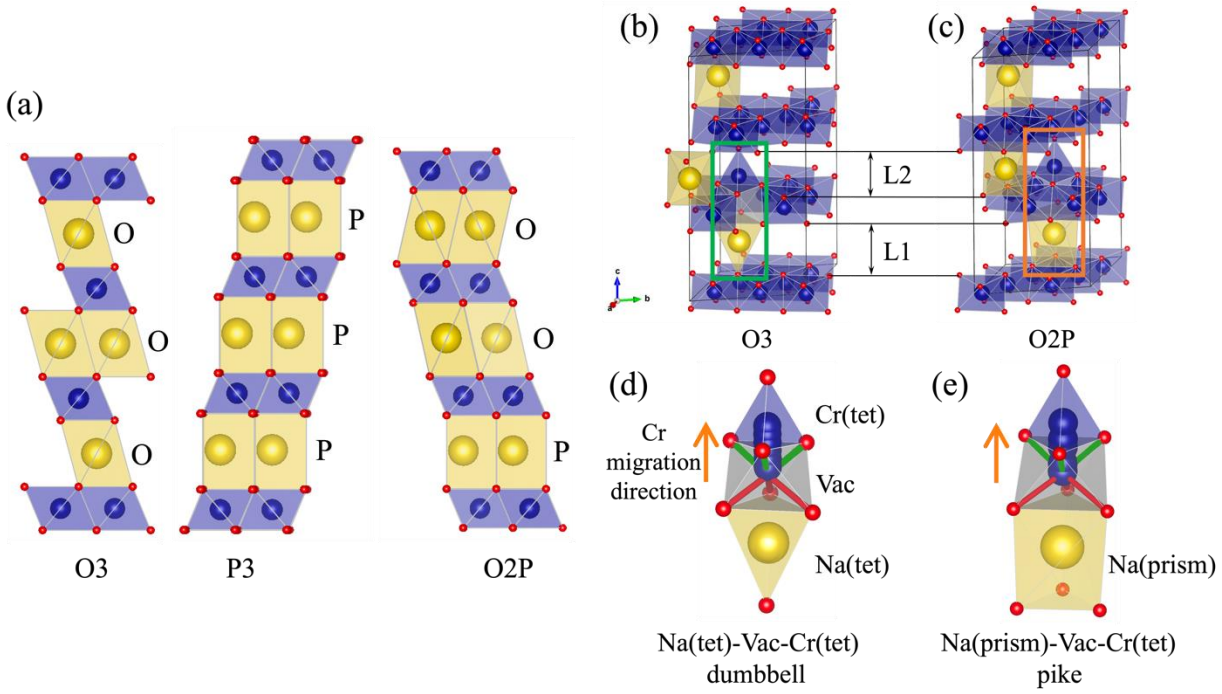

Figure 1. (a) Side view of O3, P3 and hybrid phased O2P $NaCrO_2$. Schematic of the Cr migration in (b) rhombohedral O3 and (c) O2P Na_xCrO_2 with the green and orange rectangles highlighting the low-energy local configurations in (d) and (e). L1 and L2 correspond to different Na layers in (b) and (c). The Na(tet)–Vac–Cr(tet) dumbbell and the Na(prism)–Vac–Cr(tet) pike are shown in (d) and (e) where the 3 upper (or lower) Cr–O bonds are highlighted in green (or red). The migrated Cr

tetrahedron [Cr(tet)], vacancy (Vac), Na tetrahedron [Na(tet)], and Na prism [Na(prism)] are illustrated in (d) and (e). The purple, yellow, and red balls represent the Cr, Na, and O atoms, respectively.

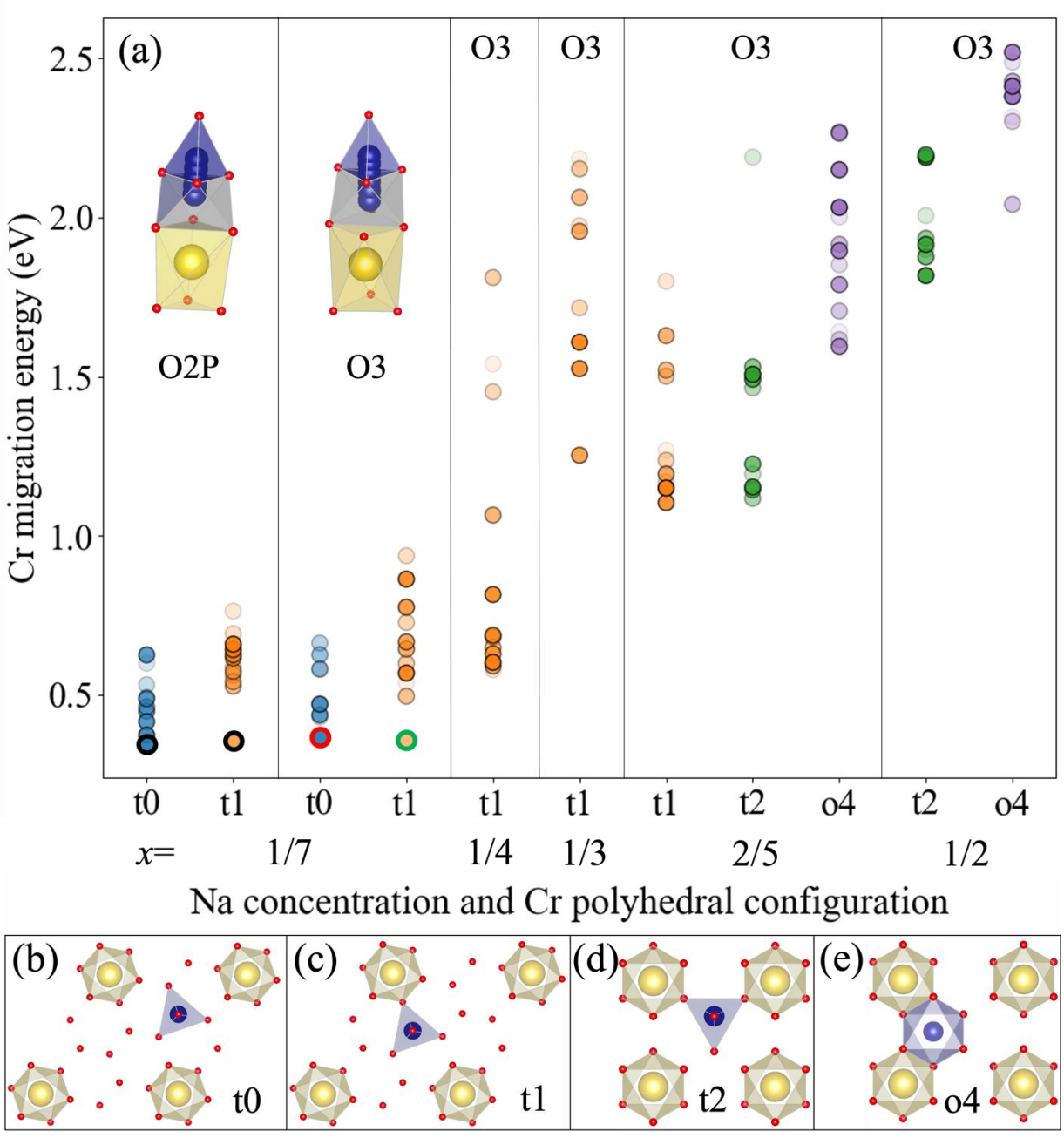

Figure 2. Calculated Cr migration energy E_{mig} for various Na concentrations (from x=1/7 to 1/2) and migrated tetrahedral or octahedral configurations in Na_xCrO_2. The Cr E_{mig} in both O2P and O3 have been calculated at x=1/7. The number in the Cr(tet) configuration label t0 (b), t1 (c), and t2 (d)

indicates the number of oxygen atoms shared between the Na octahedron and the migrated Cr(tet) within the same plane. The o4 configuration (e) indicates Cr(oct) connecting with two neighboring Na(oct) through four oxygen atoms. The transparency of each marker in (a) indicates the stability of its corresponding pristine structure, with opaque markers showing lower energies. At x=1/7, the two black bold circled structures in O2P correspond to structure I and II in Fig. 4. The red and green bold circled structures in O3 correspond to structure (c) in Fig. S3 and Structure III in Fig. 4, respectively. [27]

The Cr E_{mig} for different Na concentrations (from x=1/7 to 1/2), layer stackings (O3 and O2P at x=1/7), and in-plane geometries (t0, t1, t2, and o4) of the rhombohedral Na_xCrO_2 is presented in Fig. 2(a). In Fig. 2(b)-(e), the letter t (or o) in the in-plane geometry notation indicates Cr is tetrahedrally (or octahedrally) coordinated in L2 after migration. The following digit in the notation is the number of oxygen atoms shared between the Cr and its neighboring Na(oct). The in-plane configurations that Cr(tet) and Na(oct) share a face have very high energies from Ewald summation and were not considered for further calculations. The pristine O2P is almost as stable as O3 for x<1/4, but becomes less stable at higher x. We therefore only consider the Cr migration for O2P at x=1/7. The relative stability and lattice parameters of Na_xCrO_2 with different stackings and Na concentrations are discussed in supplemental information. [27]

Na concentration

An obvious trend in Fig. 2(a) is that Cr E_{mig} generally increases with the Na concentration. The lowest Cr E_{mig} at each composition increase gradually from 0.346 eV at x = 1/7 to 1.817 eV at x = 1/2. The large increase in Cr E_{mig} is due to the stronger cation–cation interactions when more Na are present in the L2 layer. The Cr migration to the Na layer becomes more thermodynamically unfavorable as the Na concentration increases. Since the migrated Cr is always in the high valence state (4+ and higher), [13] the cation–cation interaction gets stronger with more neighboring Na. However, unlike in layered Li TM oxides where TM migration may occur at Li concentration > 50 at.%, [44] our prediction indicates the Cr migration is less likely to happen when x>1/2 in $NaCrO_2$ [12]. At x = 1/7, the estimated Cr migration rate becomes ~10^{25} times higher than at x = 1/2, strongly enhancing the probability of Cr migrations. At low Na concentrations, the supercells suffer from greater volume shrinkage after Cr migration which can contribute to the poor cycle stability of $NaCrO_2$. [27,45–47] We tested the convergence of supercell choices on the convergence of Cr E_{mig}.

The Cr E_{mig} is affected by the stabilities of the migrated structures as well as the pristine structures. We illustrate the relative stability of pristine structures using different transparency levels to the circles in Fig. 2(a), with the opaque color representing a lower pristine energy at each stacking and in-plane geometry. For $x \leq 1/4$, more stable configurations tend to have lower Cr E_{mig}, confirming the issue of Cr interlayer migration. At $x = 1/7$, the lowest Cr E_{mig} appears in the most stable t0 configuration with both O3 and O2P. For $x > 1/4$, no correlation between pristine stability and Cr E_{mig} is found. The total energies of sampled pristine configurations differ by only about 0.1 ~ 0.2 eV/supercell, so their effect becomes negligible for $x > 1/4$ when Cr E_{mig} is much higher.

Local 3D configuration with migrated Cr

To understand the Cr migration at low Na concentrations, we then study the configurations with the lowest Cr E_{mig} at $x = 1/7$ [the 4 bold circles in Fig. 2(a)]. A typical TM migrated configuration in O3 Li compounds is a Li(tet)–Vac–TM(tet) "dumbbell" [Fig. 1(b) and (d)] [48] because Li^+ ions can occupy both the tetrahedral and octahedral site as suggested by Pauling's first rule. In Na_xCrO_2, stable dumbbell configurations also give the lowest Cr E_{mig} between $x = 1/7$ (O3–t1, green bold circle in Fig. 2) and x=2/5. No stable dumbbell configuration is found in structures with higher Cr E_{mig}. This dumbbell configuration is not stable in O3–t0 at $x = 1/7$, which is related to the in-plane geometry of the migrated Cr(tet) and Na(oct) and will be discussed in the next section.

In O2P, a different low Cr E_{mig} configuration composed of a Na(prism) in L1 after the Cr migration is discovered [Fig. 1(c) and (e)]. The local structure is a Na(prism)–Vac–Cr(tet) pike, highlighted by black bold circles in Fig. 2(a). The lowest Cr E_{mig} of the pike configuration is 0.346 eV, close to the dumbbell configuration in O3 (0.359 eV). The Na(prism) in the pike configuration stay at the nearest-neighbor site below the Cr vacancy site. Considering that the Na(tet) in the dumbbell configuration of O3 is also at the nearest neighbor site below the Cr vacancy, such a local structure is critical for a low Cr E_{mig}. In addition, this Na(prism) is distorted with a larger upper triangle area (4.70 $Å^2$) and a smaller lower triangle area (3.58 $Å^2$). The distortion in Na(prism) alleviates strong interlayer electrostatic interactions among the oxygen atoms in the perfect prismatic stacking and stabilizes the pike configuration. Another noticeable change after the Cr migration is the reduction of the L1 interlayer distance d_{L1}. d_{L1} is usually larger in O2P than in O3, which will be discussed in section 3.3.

2D in-plane Cr–Na geometry

The 2D in-plane geometry of the migrated Cr(tet) and Na(oct) in the Na layer, which can be described by the number of shared oxygen atoms between Cr(tet) and Na(oct), contributes marginally to Cr $E_{mig.}$ With a fixed oxygen stacking and Na concentration, more shared oxygen atoms usually lead to higher Cr E_{mig}. For example, in O2P and at x=1/7, the Cr E_{mig} at t1 is higher than at t0 by 0.01 to 0.137 eV. At x=2/5 and 1/2, both the lowest and the average of Cr E_{mig} at o4 are higher than t0 and t1 by over 0.4 eV. However, in O3, the lowest Cr E_{mig} at t0 is 0.013 eV higher than t1 at x=1/7 [red and green bolded circles in Fig. 2(a)]. At x=1/7, the O3–t1 configuration corresponds to the dumbbell configuration (Structure III in Fig. 4) while the O3–t0 configuration has the Na in L1 at the nearest neighbor below Vac [Fig. S3(c)]. [27] The lack of a neighboring Na in O3–t0 makes the dumbbell configuration unstable and relaxes the Na(tet) to Na(oct) in L1. As a result, while the Cr migration prefers a local Na deficient environment, this preference is also affected by the Na concentration and local 3D configuration.

3.2 The Cr migration mechanism

Next, we study the Cr migration from an octahedral site in the TM layer to a tetrahedral site in the Na layer through a shared triangular face. The Cr migration barriers for O3 and O2P at x=1/7 were calculated using the CI-NEB method. [39] For each stacking and in-plane geometry, two configurations with the lowest E_{mig} were studied. In both O2P and O3, the initial configuration of t0 is slightly lower in energy than t1 by several meV per atom. To compare the migration barriers, the energies of the initial states are shifted to 0 in Fig. 3. The Cr E_{mig} and NEB migration barriers in different layered stackings and 2D geometries are listed in Table 1.

Table 1. The Cr migration energy E_{mig}, CI-NEB Cr migration barrier, and average Cr–O bond length at pristine state for different layered stackings and 2D geometries. The data are sorted by Cr E_{mig}.

	Stacking and 2D geometry	Symbol in Fig. 3	Cr E_{mig} (eV)	Cr migration barrier (eV)	Average lower Cr–O bond length (Å)	Lower – upper Cr–O bond length (Å)
Low barrier (~1.4 eV)	O2P–t0	I	0.346	1.40	2.029	0.170
	O2P–t1	II	0.355	1.42	2.015	0.133
	O3–t1	III	0.359	1.44	2.020	0.146
Medium barrier (1.5~1.6 eV)	O2P–t1	IV	0.501	1.52	1.981	0.063
	O3–t0	V	0.429	1.56	1.995	0.082
	O3–t1	VI	0.526	1.59	1.962	0.073

High barrier (>1.7 eV)	O2P–t1	VII	0.620	1.74	1.944	0.015
	O3–t1	VIII	0.863	1.86	1.926	–0.037

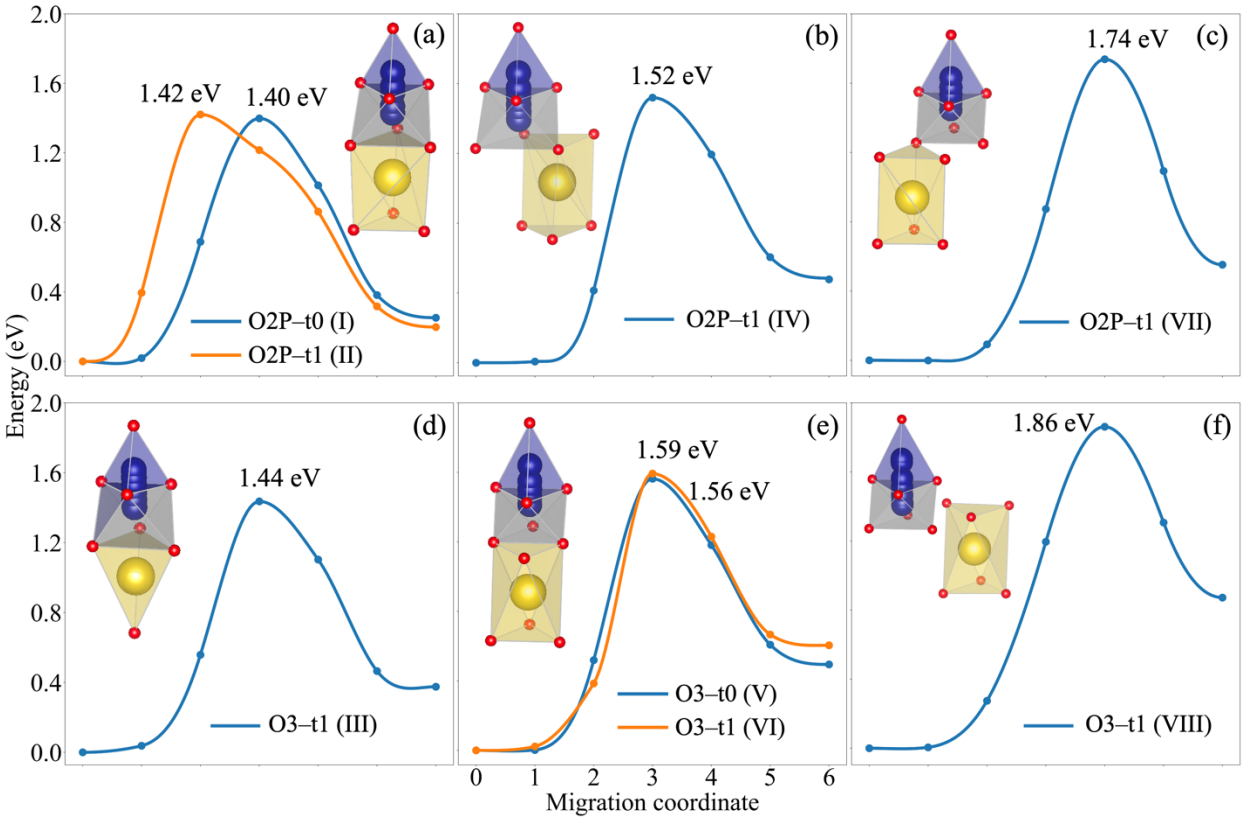

Figure 3. The calculated Cr migration barriers grouped by the Cr E_{mig} and barrier groups. Low [(a) and (d)], medium [(b) and (e)], and high [(c) and (f)] Cr migration barrier groups are presented separately. Local 3D configurations are shown as insets. The Cr E_{mig} and migration barrier are compared in Fig. 4.

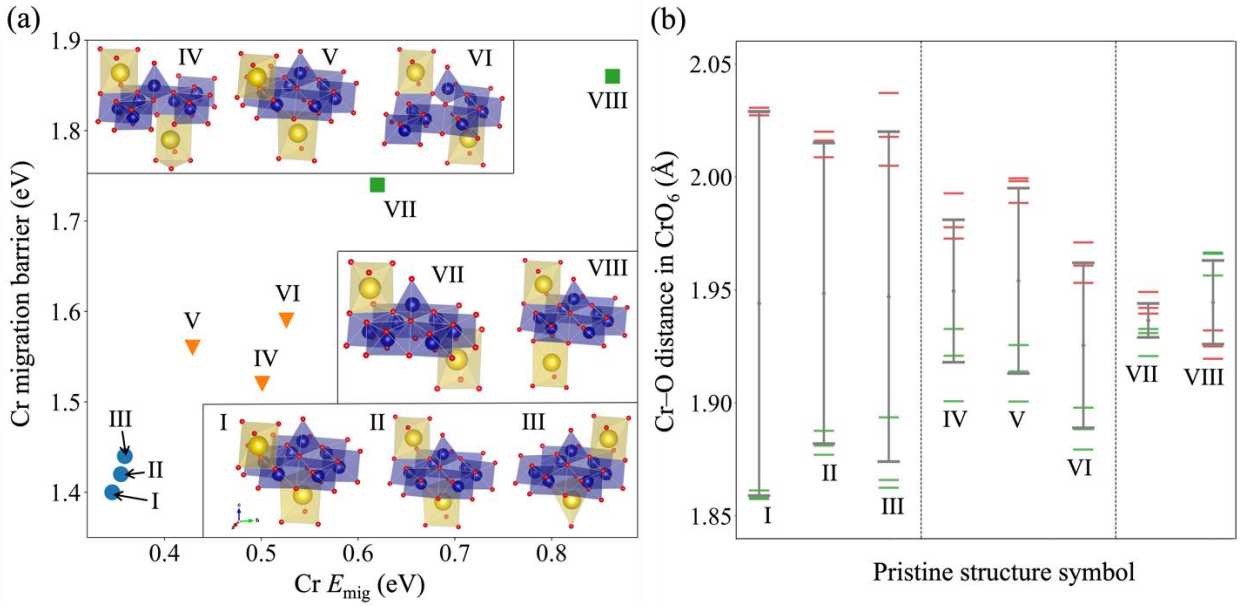

Figure 4. (a) Comparisons between Cr E_{mig} and Cr migration barriers. Data are listed in Table 1. Structure I and II (III) correspond to the black (red) bold circles in Fig. 2(a). (b) Distribution of the Cr–O bond length between the 3 lower (red bar) and 3 upper (green bar) bonds before Cr migration. The color of the different Cr–O bonds are shown in Fig. 1(d) and (e). The range of the average lower and upper bond lengths is shown in the grey capped bar.

As shown in Fig. 4(a), the Cr migration barrier is highly correlated with Cr E_{mig} in $Na_{1/7}CrO_2$. The three initial structures with the lowest Cr E_{mig} at each stacking and in-plane geometry produce similar Cr migration barrier of about 1.4 eV (blue circles). These structures include the dumbbell configuration in O3–t1 and the pike configuration in O2P for both t0 and t1. Other pristine structures with medium Cr E_{mig} at each stacking and in-plane geometry give higher Cr migration barriers of about 1.6 eV (orange triangles). The last two structures with the highest Cr E_{mig} yield the highest barrier of more than 1.7 eV (green squares). The Cr migration in Na_xCrO_2 involves the breaking of three Cr–O bonds at the initial Cr site [red rods in Fig. 1(d) and (e)]. Therefore, the average Cr–O bond length, as a metric of the Cr–O bond strength, can explain the trends in the Cr migration barrier. We list the average Cr–O bond length of the pristine structures in Table 1. Among the structures studied, a reduction of 0.05 Å in the average Cr–O bond length increases the Cr migration barrier by about 0.2 eV in the low and medium Cr E_{mig} group. Regardless of the oxygen stacking in L2, close average Cr–O bond lengths tend to produce similar Cr migration barriers. These trends are in good agreement with the experimental observation that a shorter Cr–O bond length results in better cycle stability with higher capacity retention [49]. Furthermore, the Cr–O bond length difference between the 3 lower (red) and 3 upper

(green) bonds before the Cr migration is highly correlated with Cr E_{mig} and barrier as shown in Fig. 4(b). [50] The bond length difference can be viewed as a distortion metric of the CrO_6 octahedron. With a higher degree of distortion, the Cr(oct) is more likely to migrate. In the high Cr E_{mig} group, the bond length difference is only 0.015 and –0.037 Å for O2P and O3, leading to higher Cr E_{mig} and barrier than the low Cr E_{mig} group.

Similar to its effects on Cr E_{mig}, the 2D geometry of Na and the migrated Cr only weakly affect the Cr diffusion barrier. In both O3 and O2P, the Cr diffusion barrier is almost identical for t0 and t1, differing by less than 0.03 eV. This observation agrees with the bond-breaking interpretation of the Cr migration barrier. Because the 2D geometry of Na and the migrated Cr is not directly related to the Cr–O bonds at the initial Cr site, its influence on the Cr migration barrier is small. During the migration process, the Cr atom crosses a triangular face shared by the initial Cr octahedral site and Cr(tet). The area of the shared face is about 3.9 $Å^2$ for both t0 and t1, suggesting the geometrical bottleneck for the Cr migration is also comparable for these 2D Na–Cr geometries.

Sequential migration

The formation of the low-energy dumbbell configuration in O3 requires not only the interlayer migration of Cr but also the in-plane migration of Na from an octahedral site to a tetrahedral site. We performed a CI-NEB calculation to study if these two processes take place simultaneously or sequentially (Fig. 5). In Fig. 5(c), the Na in L1 at the nearest octahedral site of the Cr (image A) first migrates to the neighboring Na(tet) under the Cr (image C) with an undercoordinated Na pentahedron forming in between (image B). The Cr then moves away from Na(tet), initializing the Cr migration. Next, a co-planar coordinated CrO_3 (Image D) appears at the highest energy of the migration process, similar to the bottleneck in the Cr only migration process in Fig. 3. Finally, the Cr moves into Cr(tet) in L2 while Na(tet) remains unchanged (image E). The overall barrier to form the dumbbell configuration is 1.56 eV in O3–t1, about the same as the calculated barrier of sole Cr migration in O3–t1(Structure VI in Fig. 4, 1.59 eV). The Na migration barrier in $Na_{1/7}CrO_2$ is only 0.19 eV in the pristine state [Fig. 6(a) and (b)], comparable to the energy change of Na migration from the initial state to image B in the sequential migration. The Cr migration energy is thus reduced by ~0.2 eV in the sequential migration compared to the Cr only migration in Structure VI. The sequential process in the dumbbell formation indicates that the Cr migration is activated by the Na migration. Limiting the in-plane migration of Na into the tetrahedral sites can be a pathway to prevent Cr migration, but this will reduce the Na diffusivity.

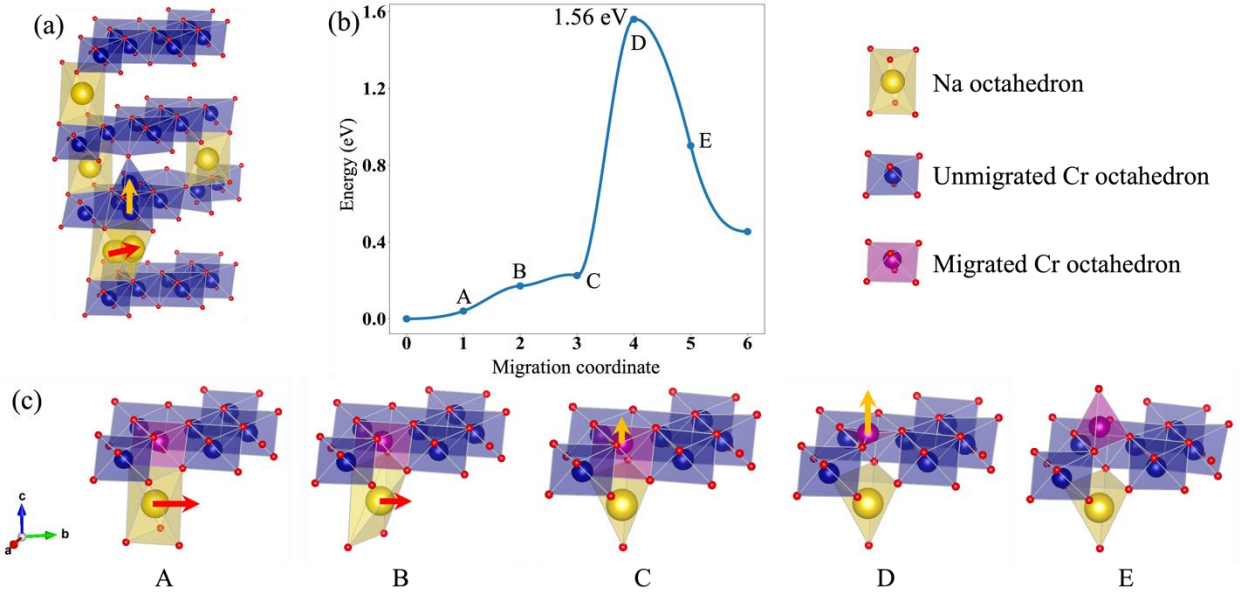

Figure 5. The sequential Na–Cr migration in O3–t1 $Na_{1/7}CrO_2$ (a) and the migration barrier (b), where the intermediate states are illustrated in (c). Image A to C correspond to the Na migration from the nearest Na(oct) site to the tetrahedron below Vac and the Cr in Vac is activated for migration in image C. Image D and E correspond to the Cr migration with the Na remains unmoved. The yellow, red, blue, and magenta ball represent Na, O, unmigrated Cr, and migrated Cr, respectively. The red and orange arrows indicate the migration direction of the Na or Cr, respectively.

The migration barrier of Na below a migrated Cr

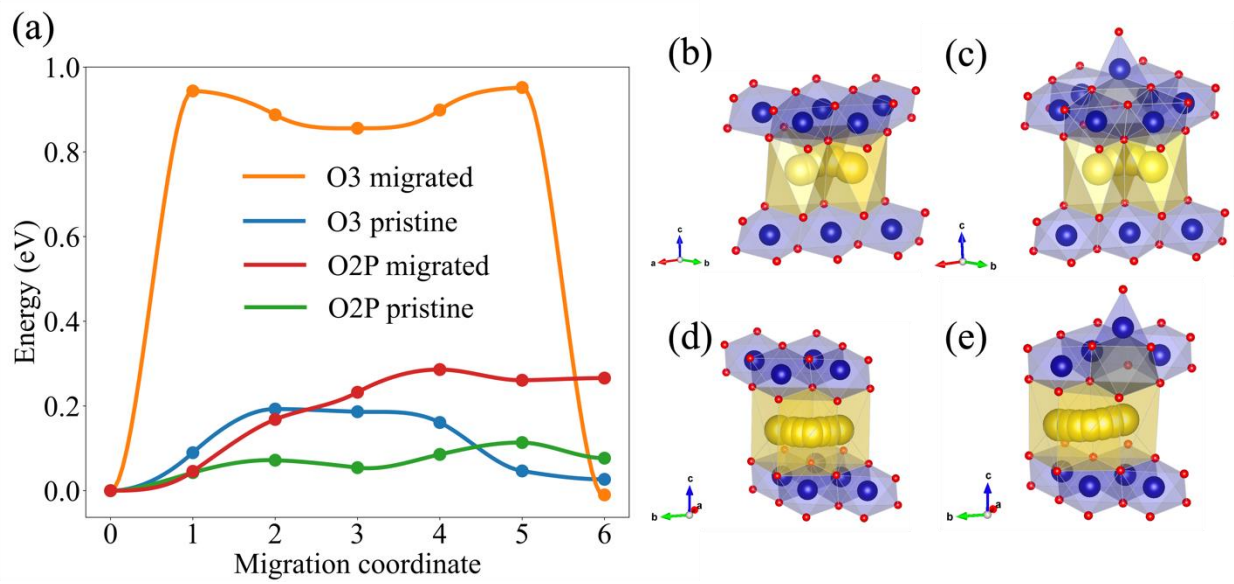

Figure 6. The Na migration barrier (a) within the O-type and P-type L1 layer in pristine [(b) and (d)] and after Cr migration [(c) and (e)]. The yellow, red, and blue ball represents the Na, O, and Cr atom, respectively. The formation of Vac after Cr migration is indicated by a grey empty octahedron.

The significant change in d_{L1} introduced by Cr migration is supposed to affect the Na migration barrier. [40] CI-NEB calculations were performed to compare the Na migration barrier in O3 and O2P before and after Cr migration (Fig. 6). The Na migration in O-type layers [Fig. 6(b) and (c)] follows the tetrahedral site hop mechanism whereas in P-type layers [Fig. 6(d) and (e)] Na migrates through the shared face between neighboring prismatic sites. [51] The Cr migration greatly increases the Na migration barrier in L1 because of contracted L1 after the Cr migration [Fig. 8(b)]. For example, the Na migration barrier increases from 0.19 eV to 0.95 eV after Cr migration in O3. It is well-known that migrated TM blocks the alkali ion diffusion pathway and leads to low diffusivity in L2 [52], low specific capacity and poor capacity retention. [45,49] In O3 $NaCrO_2$, the Na diffusion in the neighboring L1 layer of the migrated Cr is also hindered. In comparison, the Na migration barrier in the P-type layer is considerably lower (0.29 eV) after Cr migration. This difference in the Na migration barrier can contribute to the selective extraction of Na in layered biphasic compounds after TM migration. [20,21]

4. Suppression of Cr migration with dopants

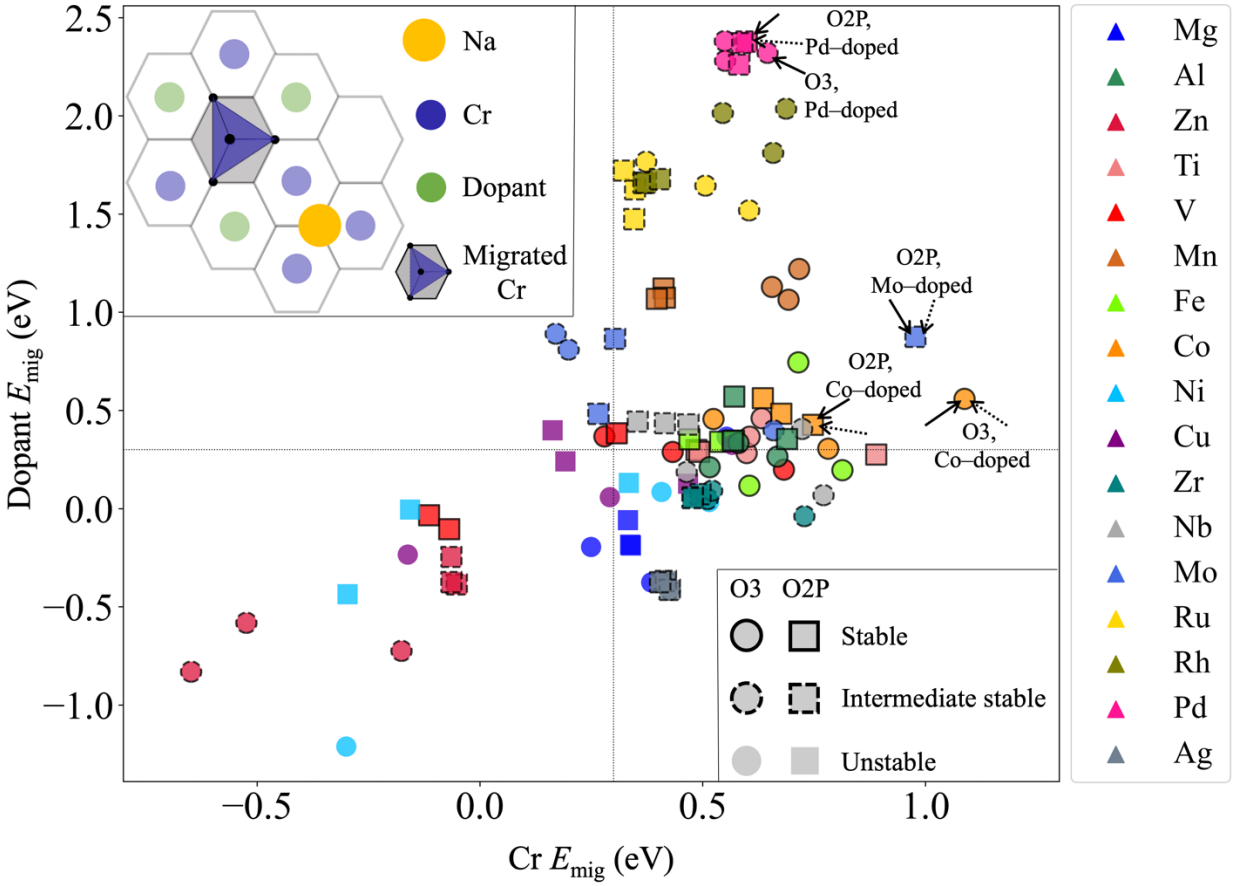

Figure 7. The E_{mig} distribution of Cr and dopants for 17 doped $Na_{1/7}CrO_2$ with O3 and O2P stacking. The dopants are non-TM (Mg, Al, and Zn) and TM (Ti, V, Mn, Fe, Co, Ni, Cu, Zr, Nb, Mo, Ru, Rh, Pd, and Ag) elements. For each dopant, 3 different Cr sites in the TM layer with Vac are considered in O3 (circle makers) and O2P (square markers), leading to a total of 6 different sites for each doped system. Relative stability of the doped pristine structure is represented by edge types. Solid, dashed, and no edge represents E_{hull} < 25, 25~50, and > 50 meV/atom. The vertical and horizontal dashed lines show an E_{mig} of 0.3 eV, which serve as a reference for Cr migration suppression. The Cr and dopant migration barriers of selected configurations with high Cr or dopant E_{mig} are indicated by solid and dashed arrows, respectively. The inset illustrates the 3 dopant sites (green circle) and migrated Cr. The migrated Cr and Na (yellow circle) is above the TM layer consisting of both Cr and dopant atoms in hexagons.

To search for dopants that can suppress the interlayer migration of Cr, the Cr-migration in doped $Na_{1/7}CrO_2$ is systematically studied. We selected common main group metals (Mg, Al, and Zn) and 3d and 4d TMs (excluding Sc, Y, Tc, and Cd) as potential dopant candidates. The doped $Na_{1/7}CrO_2$ was modeled by replacing one of the Cr atoms in the TM layer with the dopant. The Cr sites that produce face-sharing Cr(tet) and Na(oct) in L2 were not considered due to high energy of these configurations. Three symmetrically inequivalent Cr sites were studied for O3 and O2P. Fig. 7 shows the dopant E_{mig} and the Cr E_{mig} of doped $Na_{1/7}CrO_2$. The E_{hull} of the doped pristine structures are coded by edge types as solid (< 25 meV/atom, stable), dashed (25 to 50 meV/atom, intermediate stable), and no (> 50 meV/atom, unstable) edge and listed in Table S2. [27] For example, Ti–, Mo–, and Ni–doped $Na_{1/7}CrO_2$ belongs to the stable, intermediate stable, and unstable doped $Na_{1/7}CrO_2$, separately.

Most 3d TM doped $Na_{1/7}CrO_2$ are stable with their E_{hull} less than 25 meV/atom, except for Ni and Cu. Zr is the only stable 4d TM dopant while the others are intermediately stable. Non-TM dopants Mg and Zn are quite unstable. In Fig. 7, most unstable doped configurations fall in the lower left quadrant of low dopant and Cr E_{mig} (<0.3 eV), indicating that the stability of doped $NaCrO_2$ is correlated with the Cr migration. In the upper right quadrant, some dopants can suppress the Cr migration with Cr E_{mig} $\geq$ 0.5 eV and the dopant itself is also unlikely to migrate. For example, all 6 configurations of the Mn–doped $Na_{1/7}CrO_2$ are stable, and their Cr E_{mig} are ~0.5 eV and dopant E_{mig} are beyond 1 eV. One of the Co–doped $Na_{1/7}CrO_2$ configurations possesses the highest Cr E_{mig} of over 1 eV and a relatively high dopant E_{mig} of 0.5 eV. The lowest Cr E_{mig} in the Co–doped configurations is about 0.5 eV, making Co a good candidate to suppress the Cr migration. Ti– and V–doped $NaCrO_2$ can also suppress the Cr migration and the dopants themselves are stable. The dopant E_{mig} for Ru, Mo, and Pd are very high (over 1.5 eV) and their Cr E_{mig} are higher than the undoped one, but their E_{hull} is relatively high.

The effectiveness of a dopant in suppressing Cr migration is related to its valence state, [14] which can be determined from the net magnetic moment in Table S3. [27] A dopant with a valence state greater than 3+, *i.e.,* the Cr valence state in $NaCrO_2$, is considered as a high valence state dopant. Among the dopants considered, high valence state dopants [Mn^{4+}, high-spin Co^{4+}, Ti^{4+}, V^{5+}, and 4d $TM^{n+}(n\geq4)$] generally lead to high Cr E_{mig}. Meanwhile, low valence state dopants (Mg^{2+}, Zn^{2+}, low-spin Co^{3+}, Ni^{2+}, and Cu^{2+}) are generally both unstable and cannot suppress Cr migration. These findings agree with the proposed strategy using high valance state dopants to suppress Cr migration in the disproportionation-assisted phase transformation in $NaCrO_2$. [16] High valence state dopants can help to reduce the

amount of Cr^{4+}–Cr^{4+}– Cr^{4+} triplets and thus suppress the presence of Cr^{4+}. For example, the low-spin Co^{3+} produces the lowest Cr E_{mig} (0.52 eV) in Co–doped $Na_{1/7}CrO_2$, and higher Cr E_{mig} appears with the low-spin Co^{4+}. [38] Similarly, the V^{4+} in V–doped $Na_{1/7}CrO_2$ gives negative Cr E_{mig}, while the other V^{5+} produce positive Cr E_{mig} of at least 0.28 eV.

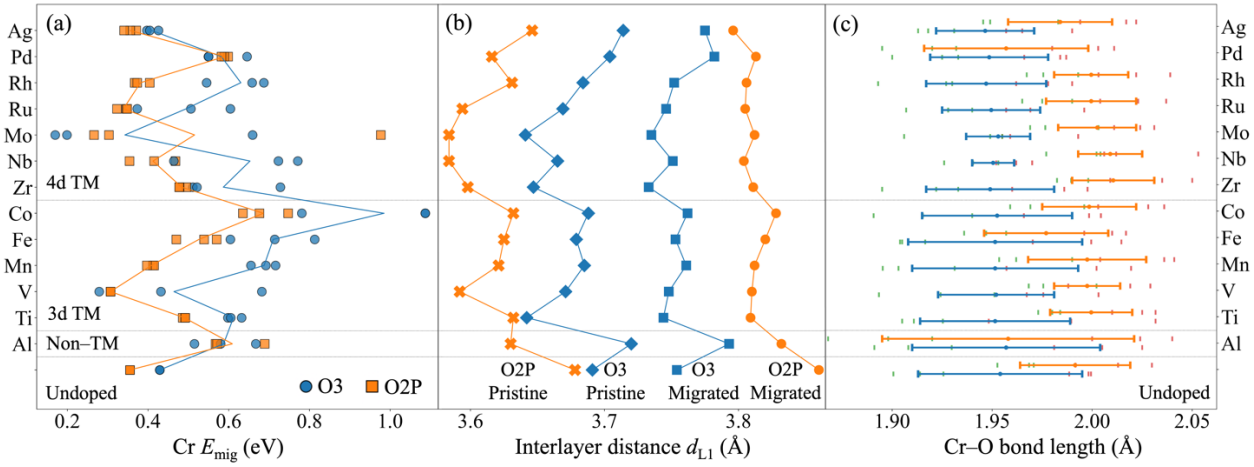

Figure 8. (a) Comparison of Cr E_{mig} in undoped and doped $Na_{1/7}CrO_2$, with the blue and orange lines corresponding to the average Cr E_{mig} for O3 and O2P, respectively. (b) The trend of the average interlayer distance d_{L1} in the pristine and Cr–migrated structures. (c) The distribution of the Cr–O bond lengths of the 3 lower (red bar in Fig. 1) and 3 upper (green bar in Fig. 1) bonds in the pristine structures. The difference of the average lower and upper bond lengths is highlighted as the blue (or orange) capped bar for O3 (or O2P). The end positions of the capped bars are the average lower and upper bond lengths and the centered circle on the capped bar shows the average of all 6 Cr–O bond lengths.

By comparing the Cr E_{mig} in undoped and doped $Na_{1/7}CrO_2$ between O3 and O2P, we notice that the Cr E_{mig} in O3 is usually higher than O2P [Fig. 8(a)]. The exceptions are the unstable dopants Mg, Zn, Cu and Ni (not shown), as well as Al and Mo that give higher Cr E_{mig} in some O2P configurations. The interlayer distance d_{L1} in $NaCrO_2$ changes differently between O3 and O2P with the Cr migration [Fig. 8(b)]. In the pristine state, regardless of the dopant species, the O2P d_{L1} is greater than the O3 d_{L1} due to the stronger O–O repulsion in the prismatically stacked layers. For example, in the undoped pristine state at x=1/7, the d_{L1} is 3.86 Å for O2P and 3.75 Å for O3. After Cr migration, the d_{L1} contraction in O2P is more severe, leading to smaller d_{L1} in O2P (3.65 Å) than in O3 (3.69 Å). The corresponding Cr E_{mig} is also lower in O2P (0.43 eV in O3 *vs.* 0.35 eV in O2P). A similar non-negligible reduction of

0.4 Å in the interlayer distance of prismatically coordinated Na layers has been reported in P2 $Na_{0.67}(Mn_{0.65}Ni_{0.15}Fe_{0.2})O_2$ at a highly charged state from experiments. [23] The change in d_{L1} becomes more obvious in doped $NaCrO_2$. As shown in Fig. 8(a) and (b), more aggressive contraction of d_{L1} in O2P is correlated with the lower Cr E_{mig} in O2P than in O3. Considering the doped $NaCrO_2$ at their pristine states have similar energies between O3 and O2P, the lower Cr E_{mig} is largely caused by the lower energy of the O2P Cr-migrated structures manifested by the change in d_{L1}.

In addition to d_{L1}, the pristine Cr–O bond length in CrO_6 octahedron is another descriptor for the Cr E_{mig} differences between O3 and O2P. In Fig. 8(c), the bond lengths of the 3 upper and lower Cr–O bonds are presented by the vertical green and red bars, respectively. The ends of the horizontal blue (or orange) capped bars represent the average value of the lower and upper bond lengths for O3 (or O2P). The position of the centered circle on the capped bar corresponds to the average bond length, and the span of the capped bar describes the difference between the average lower and upper bond length. A longer span suggests Cr(oct) shifts away from the center of the CrO_6 octahedron and can be viewed as creating a higher degree of distortion of the octahedron. Except for Al, the relative positions of most orange bars appear to the right of the blue bars, indicating longer Cr–O bonds in O2P. Since longer equilibrium Cr–O bonds are generally weaker, the Cr E_{mig} is reduced in O2P. In Al–doped $NaCrO_2$, the positions of the blue and orange bars are almost identical, while the longer span of the orange bars indicates higher distortion of the CrO_6 octahedron in O2P. As a result, the Cr E_{mig} for Al–doped $NaCrO_2$ are higher in O2P than O3. Furthermore, whether the doped $Na_{1/7}CrO_2$ has higher Cr E_{mig} over the undoped one is correlated with the span of bars. For example, the span of the capped bar in undoped O3 and O2P is 0.08 and 0.06 Å, respectively. The span becomes smaller for the doped $Na_{1/7}CrO_2$ that has relatively high Cr E_{mig} due to the reduced distortion of CrO_6 octahedron. Most 4d TM doped $Na_{1/7}CrO_2$ show a reduced span of the capped bars with respect to undoped $Na_{1/7}CrO_2$, suggesting potentials for suppressing the Cr migration.

The dopants that produce high Cr or dopant E_{mig} were further verified with diffusion barrier calculations. We first calculated the Cr migration barrier in Co–, Mo–, and Pd–doped $Na_{1/7}CrO_2$ because Co and Mo leads to the highest Cr E_{mig} in O3 and O2P, and Pd has the highest dopant E_{mig} among the studied systems (Fig. S5). [27] The calculated Cr migration barriers in these doped $Na_{1/7}CrO_2$ are all higher than the undoped systems as shown in Table S4. [27] For example, the Cr migration barrier in O2P Mo–doped $Na_{1/7}CrO_2$ is 1.63 eV, higher than the undoped one by 0.21 eV. The increase in the Cr migration barrier is correlated with the increase in Cr E_{mig}. Then, the dopant

migration barriers were calculated to study if any preference exists for the Cr or dopant migration. Among them, the lowest dopant migration barrier is 1.85 eV in Mo–doped $Na_{1/7}CrO_2$, higher than the Cr migration barrier [Fig. S5(e)]. [27] In addition, we studied whether the Mo migration barrier will be affected by the Na position in L1 [Fig. S5(e) and (f)]. [27] The Mo migration barrier is 1.85 eV when Na in L1 stays at the nearest neighbor to Vac, lower than the barrier when Na stays at the next nearest neighbor by around 0.1 eV. This trend is identical as the Cr migration barrier in Fig. 4. Although the calculation of dopant migration barriers is by no means exhaustive, we proved that these dopants have relatively higher migration barrier than the Cr migration barrier.

5. Conclusion

First-principles calculations have been performed to study the Cr migration in layered O3 and O2P $NaCrO_2$. The effect of Na concentrations, in-plane migrated Cr–Na geometries, and local configurations on the Cr E_{mig} are systematically investigated. Low Na concentrations and Na staying at the near neighbor below the migrated Cr usually leads to low Cr E_{mig}. Two typical Cr–migrated configurations with low Cr E_{mig} (dumbbell and pike) are identified for O3 and O2P. The Cr E_{mig} are found positively correlated to the CI–NEB calculated Cr migration barriers. The dumbbell and pike configuration produces similar Cr migration barriers, which are the lowest among the studied configurations. Meanwhile, the Cr migration are found to be activated by the Na migration, following a sequential migration process. In addition, the Cr migration severely contracts the neighboring Na layer and leads to increased Na migration barrier. The Cr and dopant E_{mig} for 17 doped systems were computed. Among them, Co and several other high valence state TM dopants can effectively suppress the Cr migration and the dopants have higher migration barrier than Cr. Non–TM Mg and Zn are unstable for doping and cannot suppress Cr migration. Two structural descriptors are related to the Cr E_{mig}, the interlayer distance d_{L1} and the distortion of the CrO_6. Structures with larger d_{L1} and more severe distortion are usually easier for Cr migration.

Acknowledgements

The authors gratefully acknowledge the support by the National Science Foundation under Grant No. DMR-1709959 and DMR-1945380. This research used resources of the National Energy Research Scientific Computing Center (NERSC), a U.S. Department of Energy Office of Science User Facility operated under Contract No. DE-AC02-05CH11231. This work used the Extreme Science and Engineering Discovery Environment (XSEDE), which is supported by National Science Foundation grant number ACI-1548562.

References

[1] C. Delmas, *Sodium and Sodium-Ion Batteries: 50 Years of Research*, Adv. Energy Mater. **8**, 1703137 (2018).

[2] N. Yabuuchi, K. Kubota, M. Dahbi, and S. Komaba, *Research Development on Sodium-Ion Batteries*, Chem. Rev. **114**, 11636 (2014).

[3] S. Komaba, C. Takei, T. Nakayama, A. Ogata, and N. Yabuuchi, *Electrochemical Intercalation Activity of Layered NaCrO2 vs. LiCrO2*, Electrochem. Commun. **12**, 355 (2010).

[4] D. Wu, X. Li, B. Xu, N. Twu, L. Liu, and G. Ceder, *NaTiO2: A Layered Anode Material for Sodium-Ion Batteries*, Energy Environ. Sci. **8**, 195 (2014).

[5] X. Ma, H. Chen, and G. Ceder, *Electrochemical Properties of Monoclinic NaMnO2*, J. Electrochem. Soc. **158**, A1307 (2011).

[6] P. Vassilaras, X. Ma, X. Li, and G. Ceder, *Electrochemical Properties of Monoclinic NaNiO 2* , J. Electrochem. Soc. **160**, A207 (2013).

[7] S. Kikkawa, S. Miyazaki, and M. Koizumi, *Deintercalated NaCoO2 and LiCoO2*, J. Solid State Chem. **62**, 35 (1986).

[8] C. Didier, M. Guignard, C. Denage, O. Szajwaj, S. Ito, I. Saadoune, J. Darriet, and C. Delmas, *Electrochemical Na-Deintercalation from NaVO2*, Electrochem. Solid-State Lett. **14**, A75 (2011).

[9] Y. Takeda, K. Nakahara, M. Nishijima, N. Imanishi, O. Yamamoto, M. Takano, and R. Kanno, *Sodium Deintercalation from Sodium Iron Oxide*, Mater. Res. Bull. **29**, 659 (1994).

[10] C. Delmas, C. Fouassier, and P. Hagenmuller, *Structural Classification and Properties of the Layered Oxides*, Phys. B+C **99**, 81 (1980).

[11] A. Maazaz, C. Delmas, and P. Hagenmuller, *A Study of the Na x TiO2 System by Electrochemical Deintercalation*, J. Incl. Phenom. 1983 11 **1**, 45 (1983).

[12] S. Kim, X. Ma, S. P. Ong, and G. Ceder, *A Comparison of Destabilization Mechanisms of the Layered Na XMO 2 and Li XMO 2 Compounds upon Alkali De-Intercalation*, Phys. Chem. Chem. Phys. **14**, 15571 (2012).

[13] K. Kubota, I. Ikeuchi, T. Nakayama, C. Takei, N. Yabuuchi, H. Shiiba, M. Nakayama, and S. Komaba, *New Insight into Structural Evolution in Layered NaCrO2 during Electrochemical Sodium Extraction*, J. Phys. Chem. C **119**, 166 (2015).

[14] D. Wang et al., *Intrinsic Role of Cationic Substitution in Tuning Li/Ni Mixing in High-Ni Layered Oxides*, Chem. Mater. **31**, 2731 (2019).

[15] Y. Li, Y. Gao, X. Wang, X. Shen, Q. Kong, R. Yu, G. Lu, Z. Wang, and L. Chen, *Iron Migration and Oxygen Oxidation during Sodium Extraction from NaFeO2*, Nano Energy **47**, 519 (2018).

[16] S. H. Bo, X. Li, A. J. Toumar, and G. Ceder, *Layered-to-Rock-Salt Transformation in Desodiated NaxCrO2 (X<0.4)*, Chem. Mater. **28**, 1419 (2016).

[17] S.-W. Kim, D.-H. Seo, X. Ma, G. Ceder, and K. Kang, *Electrode Materials for Rechargeable Sodium-Ion Batteries: Potential Alternatives to Current Lithium-Ion Batteries*, Adv. Energy Mater. **2**, 710 (2012).

[18] Y. Lei, X. Li, L. Liu, and G. Ceder, *Synthesis and Stoichiometry of Different Layered Sodium Cobalt Oxides*, Chem. Mater. **26**, 5288 (2014).

[19] A. K. Paidi et al., *Unravelling the Nature of the Intrinsic Complex Structure of Binary-Phase Na-Layered Oxides*, Adv. Mater. 2202137 (2022).

[20] N. Yabuuchi, M. Kajiyama, J. Iwatate, H. Nishikawa, S. Hitomi, R. Okuyama, R. Usui, Y. Yamada, and S. Komaba, *P2-Type Nax [Fe1/2 Mn1/2]O2 Made from Earth-Abundant Elements for Rechargeable Na Batteries*, Nat. Mater. **11**, 512 (2012).

[21] J. C. Kim et al., *Direct Observation of Alternating Octahedral and Prismatic Sodium Layers in O3‐Type Transition Metal Oxides*, Adv. Energy Mater. **10**, 2001151 (2020).

[22] J. W. Somerville et al., *Nature of the "z"-Phase in Layered Na-Ion Battery Cathodes*, Energy Environ. Sci. **12**, 2223 (2019).

[23] E. Talaie, V. Duffort, H. L. Smith, B. Fultz, and L. F. Nazar, *Structure of the High Voltage Phase of Layered P2-Na2/3-z[Mn1/2Fe1/2]O2 and the Positive Effect of Ni Substitution on Its Stability*, Energy Environ. Sci. **8**, 2512 (2015).

[24] K. Xi et al., *A High-Performance Layered Cr-Based Cathode for Sodium-Ion Batteries*, Nano Energy **67**, 104215 (2020).

[25] S. P. Ong, V. L. Chevrier, G. Hautier, A. Jain, C. Moore, S. Kim, X. Ma, and G. Ceder, *Voltage, Stability and Diffusion Barrier Differences between Sodium-Ion and Lithium-Ion*

Intercalation Materials, Energy Environ. Sci. **4**, 3680 (2011).

[26] M. H. Cao, Y. Wang, Z. Shadike, J. L. Yue, E. Hu, S. M. Bak, Y. N. Zhou, X. Q. Yang, and Z. W. Fu, *Suppressing the Chromium Disproportionation Reaction in O3-Type Layered Cathode Materials for High Capacity Sodium-Ion Batteries*, J. Mater. Chem. A **5**, 5442 (2017).

[27] *See Supplemental Material at []* for the comparison of single and hybrid phases, Ewald summation screening, low energy Cr migrated structures and Cr migration barriers under the effect of dopants.

[28] A. Y. Toukmaji and J. A. Board, *Ewald Summation Techniques in Perspective: A Survey*, Computer Physics Communications.

[29] P. E. Blöchl, *Projector Augmented-Wave Method*, Phys. Rev. B **50**, 17953 (1994).

[30] G. Kresse and J. Furthmüller, *Efficient Iterative Schemes for Ab Initio Total-Energy Calculations Using a Plane-Wave Basis Set*, Phys. Rev. B - Condens. Matter Mater. Phys. **54**, 11169 (1996).

[31] G. Kresse and J. Furthmüller, *Efficiency of Ab-Initio Total Energy Calculations for Metals and Semiconductors Using a Plane-Wave Basis Set*, Comput. Mater. Sci. **6**, 15 (1996).

[32] J. P. Perdew, M. Ernzerhof, and K. Burke, *Rationale for Mixing Exact Exchange with Density Functional Approximations*, J. Chem. Phys. **105**, 9982 (1996).

[33] J. P. Perdew, K. Burke, and M. Ernzerhof, *Generalized Gradient Approximation Made Simple*, Phys. Rev. Lett. **77**, 3865 (1996).

[34] V. I. Anisimov, F. Aryasetiawan, and A. I. Lichtenstein, *First-Principles Calculations of the Electronic Structure and Spectra of Strongly Correlated Systems: The LDA + U Method*, Journal of Physics Condensed Matter.

[35] L. Wang, T. Maxisch, and G. Ceder, *Oxidation Energies of Transition Metal Oxides within the GGA+U Framework*, Phys. Rev. B - Condens. Matter Mater. Phys. **73**, 195107 (2006).

[36] A. Jain et al., *Commentary: The Materials Project: A Materials Genome Approach to Accelerating Materials Innovation*, APL Materials.

[37] A. Jain, G. Hautier, S. P. Ong, C. J. Moore, C. C. Fischer, K. A. Persson, and G. Ceder, *Formation Enthalpies by Mixing GGA and GGA <span Class*, Phys. Rev. B **84**, 045115 (2011).

[38] M. Aykol, S. Kim, and C. Wolverton, *Van Der Waals Interactions in Layered Lithium Cobalt Oxides*, J. Phys. Chem. C **119**, 19053 (2015).

[39] G. Henkelman, B. P. Uberuaga, and H. Jónsson, *Climbing Image Nudged Elastic Band Method for Finding Saddle Points and Minimum Energy Paths*, J. Chem. Phys. **113**, 9901 (2000).

[40] J. Wei, L. Shaw, and W. Chen, *First-Principles Prediction of Na Diffusivity in Doped NaCrO2Layered Cathode Materials with van Der Waals Interactions*, J. Phys. Chem. C **124**, 12239 (2020).

[41] J. Reed and G. Ceder, *Role of Electronic Structure in the Susceptibility of Metastable Transition-Metal Oxide Structures to Transformation*, Chem. Rev. **104**, 4513 (2004).

[42] K. Ku et al., *A New Lithium Diffusion Model in Layered Oxides Based on Asymmetric but Reversible Transition Metal Migration*, Energy Environ. Sci. **13**, 1269 (2020).

[43] D. Eum et al., *Voltage Decay and Redox Asymmetry Mitigation by Reversible Cation Migration in Lithium-Rich Layered Oxide Electrodes*, Nat. Mater. **19**, 419 (2020).

[44] D. Qian, B. Xu, M. Chi, and Y. S. Meng, *Uncovering the Roles of Oxygen Vacancies in Cation Migration in Lithium Excess Layered Oxides*, in *Physical Chemistry Chemical Physics*, Vol. 16 (2014), pp. 14665–14668.

[45] M. Luo, A. L. Ortiz, and L. L. Shaw, *Enhancing the Electrochemical Performance of NaCrO2through Structural Defect Control*, ACS Appl. Energy Mater. **3**, 7216 (2020).

[46] C.-Y. Yu, J.-S. Park, H.-G. Jung, K.-Y. Chung, D. Aurbach, Y.-K. Sun, and S.-T. Myung, *NaCrO2 Cathode for High-Rate Sodium-Ion Batteries*, Energy Environ. Sci. **8**, 2019 (2015).

[47] Y. Wang, X. Yu, S. Xu, J. Bai, R. Xiao, Y.-S. Hu, H. Li, X.-Q. Yang, L. Chen, and X. Huang, *A Zero-Strain Layered Metal Oxide as the Negative Electrode for Long-Life Sodium-Ion Batteries*, Nat. Commun. 2013 41 **4**, 1 (2013).

[48] J. Reed, G. Ceder, and A. Van Der Ven, *Layered-to-Spinel Phase Transition in LixMnO2*, Electrochem. Solid-State Lett. **4**, A78 (2001).

[49] M. Sawicki, A. L. Ortiz, M. Luo, and L. L. Shaw, *Structural-Defect-Controlled Electrochemical Performance of Sodium Ion Batteries with NaCrO2 Cathodes*, ChemElectroChem **4**, 3222 (2017).

[50] X. Li, Y. Wang, D. Wu, L. Liu, S. H. Bo, and G. Ceder, *Jahn-Teller Assisted Na Diffusion*

for High Performance Na Ion Batteries, Chem. Mater. **28**, 6575 (2016).

[51] A. Van der Ven and G. Ceder, *Lithium Diffusion Mechanisms in Layered Intercalation Compounds*, J. Power Sources **97**–**98**, 529 (2001).

[52] B. Silván, E. Gonzalo, L. Djuandhi, N. Sharma, F. Fauth, and D. Saurel, *On the Dynamics of Transition Metal Migration and Its Impact on the Performance of Layered Oxides for Sodium-Ion Batteries: NaFeO2 as a Case Study*, J. Mater. Chem. A **6**, 15132 (2018).